











Bayesian real-time classification of multi-messenger electromagnetic and gravitational-wave observations

Marina Berbel ^{1,*} Miquel Miravet-Tenés ^{2,†} Sushant Sharma Chaudhary ^{3,‡}
Simone Albanesi ⁴ Marco Cavaglià ³ Lorena Magaña Zertuche ⁵ Dimitra Tseneklidou ^{2,6} Yanyan Zheng ³
Michael W. Coughlin ⁷ and Andrew Toivonen ⁷

¹*Departament de Matemàtiques, Universitat Autònoma de Barcelona, 08193 Bellaterra, Spain*

²*Departament d'Astronomia i Astrofísica, Universitat de València, Dr. Moliner 50, 46100, Burjassot (València), Spain*

³*Institute of Multi-messenger Astrophysics and Cosmology & Physics Department,
Missouri University of Science and Technology, Rolla, MO 65409, USA*

⁴*Dipartimento di Fisica, Università di Torino & INFN Sezione di Torino, via P. Giuria 1, 10125 Torino, Italy*

⁵*Department of Physics and Astronomy, University of Mississippi, University, Mississippi 38677, USA*

⁶*Theoretical Astrophysics Department, Eberhard-Karls University of Tübingen, Tübingen 72076, Germany*

⁷*School of Physics and Astronomy, University of Minnesota, Minneapolis, MN 55455, USA*

(Dated: April 15, 2024)

Because of the electromagnetic radiation produced during the merger, compact binary coalescences with neutron stars may result in multi-messenger observations. In order to follow up on the gravitational-wave signal with electromagnetic telescopes, it is critical to promptly identify the properties of these sources. This identification must rely on the properties of the progenitor source, such as the component masses and spins, as determined by low-latency detection pipelines in real time. The output of these pipelines, however, might be biased, which could decrease the accuracy of parameter recovery. Machine learning algorithms are used to correct this bias. In this work, we revisit this problem and discuss two new implementations of supervised machine learning algorithms, K-Nearest Neighbors and Random Forest, which are able to predict the presence of a neutron star and post-merger matter remnant in low-latency compact binary coalescence searches across different search pipelines and data sets. Additionally, we present a novel approach for calculating the Bayesian probabilities for these two metrics. Instead of metric scores derived from binary machine learning classifiers, our scheme is designed to provide the astronomy community well-defined probabilities. This would deliver a more direct and easily interpretable product to assist electromagnetic telescopes in deciding whether to follow up on gravitational-wave events in real time.

I. INTRODUCTION

The first detection of a gravitational-wave (GW) signal from a pair of coalescing black holes in 2015 and the first observation of a coalescing binary neutron star system two years later have established multi-messenger astronomy (MMA) as a powerful tool for the exploration of the cosmos [1–3]. The third LIGO, Virgo, and KAGRA (LVK) catalog of transient GW signals (GWTC-3) [4] has shown that GW astronomy has entered its mature phase, becoming a true observational branch of astronomy. MMA allows scientists to explore in depth the origin and structure of black holes (BHs) [5–7], neutron stars (NSs) [8–10] and gamma-ray bursts (GRBs) [11, 12], test general relativity [13–16], probe the fundamental nature of gravity [17–19], and measure the evolution of the universe [20, 21].

A wealth of new detections is being amassed to achieve these science goals [22, 23]. The rate of detections in LVK's fourth observing run (O4) is close to one per day and is expected to further increase in the fifth observing run (O5) [24]. Over the course of O4 and the next observing runs, the LVK collaboration will analyze hundreds of

binary black hole (BBH) and dozens of binary neutron star (BNS) and neutron star and black hole (NSBH) detections, several of which could be MMA sources. Among the challenges that this new phase of GW astronomy brings is the necessity to coordinate the activities of electromagnetic (EM) and GW observatories in real time.

One of the most interesting areas of study in MMA is the physics of gravity-matter interaction in GW sources. Tidally disrupted matter in systems with a NS may form a high-temperature accretion disk around the BH and trigger the creation of a prompt EM emission in the form of a short GRB. If the system ejecta are unbound, r-process nucleosynthesis may lead to a kilonova [25–30]. These phenomena could also arise in BNS post-mergers through the expulsion of neutron-rich material even when tidal forces are weak [31–37]. The presence of a post-merger matter remnant, which results in an EM signature or a prompt collapse, is a common factor in all of these scenarios. Determining the potential of a GW source to become an EM emitter and enabling coincident observations of these systems by EM and GW observatories in low latency are crucial for the success of MMA.

The LVK employs different matched-filtering pipelines for low-latency GW searches [38–44]. These searches are based on discrete template banks of compact binary coalescence (CBC) waveforms that provide, among other parameters, the component masses and the dimensionless

* mberbel@mat.uab.cat

† miquel.miravet@uv.es

‡ sscwrk@umsystem.edu

(anti-)aligned spins of the objects along the orbital angular momentum. These parameters can be used to determine the EM properties of GW candidates in real time through empirical fits of numerical relativity (NR) simulations [45, 46]. Alerts of candidate GW events that included two EM-property metrics identifying whether the CBC system contains a NS, **HasNS**, and a post-merger matter remnant, **HasRemnant**, were issued in third observing run (O3) with a median latency of the order of a few minutes after detection. Alerts with similar content continue to be issued in O4 with even lower latency. Additionally, LVK’s O4 alerts include a measure of the **HasMassGap** property, i.e., the likelihood that one of the source compact objects has a mass in the lower-mass gap region between NSs and BHs [47] (see the LVK online user guide [48]).

Classification of GW candidate events in low latency poses several challenges as the need for accuracy contrasts with the urgency to issue the information as quickly as possible. The approach taken by the LVK so far has been to use a specific implementation of a supervised KNeighborClassifier (KNN) machine learning (ML) algorithm [49] with input from the detection pipelines and equation of state (EOS) models to generate independent **HasNS** and **HasRemnant** binary classification *scores* [50]. The KNN model is trained on a broad set of synthetic CBC signals injected in real detector noise from the second observing run (O2). The advantage of this scheme relies on its capability to handle the statistical systematic uncertainties in the parameters recovered by the search pipelines. This approach allowed for a marked improvement in speed compared to the semi-analytic effective Fisher formalism method that was deployed in O2.

In this work, we revisit the problem of the real-time production of **HasNS** and **HasRemnant** *probability* metrics with the aim of further improving the latency and performance of the current LVK ML-based scheme [50]. In the current implementation, the validity of the classification outcome for an event is assessed through elements of the algorithm’s confusion matrix and its Receiver Operating Characteristic (ROC) curve. For example, given a positive prediction, the LVK collaborations define a “score” that this prediction is correct as the true positive rate (TPR) for the given data set. However, there is no quantity in the algorithm’s confusion matrix that defines a probability in the strictest sense. A second limitation of the current **HasNS** and **HasRemnant** classification implementation is the fact that the **HasNS** and **HasRemnant** labels are treated as independent variables. In reality, the probability of the formation of tidally disrupted matter, i.e. an EM bright event, is always smaller than the probability of the system hosting a NS. Therefore, the **HasNS** and **HasRemnant** labels cannot be treated as disjoint. In the current LVK implementation, this physical condition is data-based rather than being mathematically defined, i.e., the algorithm potentially allows for violations and the absence of inversions is only checked a posteriori through (coarse) parameter sweeps. One of the main purposes of this work is to go beyond the above scheme and calcu-

late true *conditional Bayesian probabilities* for **HasNS** and **HasRemnant**.

To achieve this, we design a new classification scheme and perform a thorough study and comparison of two ML algorithms. We first implement a definition for conditional **HasNS** and **HasRemnant** metrics that incorporates *ab initio* the physical requirement that a system with a post-merger matter remnant must necessarily contain a NS. Then we calculate *Bayesian probabilities* for **HasNS** and **HasRemnant**. We also implement a marginalization procedure over a set of EOS that minimizes possible systematics arising from the use of a single EOS. Finally, we test the performance of the scheme and the algorithms on synthetic O3 signals and confident GW detections from the latest GWTC-3 catalog.

The structure of the paper is as follows. Section II introduces the classification algorithms. Bayesian probabilities for **HasNS** and **HasRemnant** and the labeling scheme are defined in Sec. III. The data set is described in Sec. III B. Results and algorithm comparisons are reported in Sec. IV. Conclusions and future developments are presented in Sec. V.

II. CLASSIFICATION ALGORITHMS

We consider two alternative algorithms for unsupervised classification: KNN and random forest (RF). These methods were chosen because of their versatility, ease of implementation in low-latency, and comparison with the algorithms currently being used by the LVK (KNN for **HasNS** and **HasRemnant**, RF for **HasMassGap**). In this section, we briefly describe the relevant features of the algorithms and their implementation.

K-Nearest Neighbors

K-Nearest Neighbors is a non-parametric, supervised algorithm [51, 52] that uses the fact that similar points in a data set are “near” each other in their parameter space. When it is applied to classification problems [53], the algorithm is usually renamed KNN. The algorithm captures the idea of similarity between points by computing the distance between each point in a training set and its neighbors according to a pre-determined metric. Next, it sorts the neighbors in ascending order based on their distance to the testing point. By choosing the top K neighbors from the sorted array, KNN assigns the label to the testing point that corresponds to the most frequent neighbor.

In this work, we use the open-source Python KNN implementation of scikit-learn [49]. We fix the algorithm hyperparameters by cross-validating over the data set and obtain the highest accuracy. Throughout our analysis we use $K = 8$ neighbors, the Manhattan metric, the BallTree algorithm and the neighbors are weighted by the inverse of their distance to the event. This configuration differs

from the LVK's current implementation, which employs the Mahalanobis metric and $K = 2n + 1 = 11$ neighbors, where n is the number of features. Our configuration is the optimal choice for the new labeling scheme that is presented in Sect. III C).

Random Forest

RF is a classification method based on an ensemble of decision trees. The trees are hierarchical models that make decisions by recursively splitting the data at the separation nodes into different categories based on the values of features. Each tree in the forest is trained independently. To classify a data point, each tree predicts a category and the algorithm assigns the one that has been chosen the most. RF is known for its parallelization capabilities, as computations inside each tree are independent from the rest. An RF algorithm is usually trained using bootstrapping, a technique that randomly assigns subsets of the training data set to each tree. This helps prevent overfitting, as each individual classifier is not exposed to the same data, and encourages pattern recognition by studying the same data from different subsets. The model's performance on the given data set can be optimized by tuning the input hyperparameters.

In this work, we use the open-source Python RF implementation of scikit-learn [49]. The main tunable hyperparameters are the number of trees, the maximum allowed depth, and the information gain criteria used at splitting. Similar to KNN, we choose the algorithm's optimal hyperparameters by measuring the accuracy in the testing set. We use 50 trees in the forest, with a maximum depth of 15, and the maximum number of features considered in a node is the square root of the total number of features.

III. PROBABILITY AND LABELING SCHEME

Bayesian probabilities for the `HasNS` and `HasRemnant` metrics can be defined using the results of the KNN and RF algorithms, namely the fraction of KNN's neighbors and RF's trees that predict a given label. In this section, we define the probabilities and explain how to derive them from a data set of simulated signals.

A. Definition of Bayesian Probabilities

Let us define the probability of a system having a NS (`HasNS:TRUE`) and being EM bright (`HasRemnant:TRUE`), given an event X and the classifier outcome on the detection pipeline output, \mathbf{A}_X , as $P(\text{HasNS}|\mathbf{A}_X)$ and $P(\text{HasRemnant}|\mathbf{A}_X)$, respectively. The classifier outcome can be understood as a map $A : \mathbf{X} \rightarrow \mathbf{A}_X$, where \mathbf{X} is a vector that identifies the output of the detection pipeline and \mathbf{A}_X is a vector that uniquely identifies the algorithm's output for \mathbf{X} .

Since a system can be EM-bright only when a NS is present in the system, the condition $P(\text{HasRemnant}|\mathbf{A}_X) \leq P(\text{HasNS}|\mathbf{A}_X)$ must hold. However, if the probabilities are calculated disjointly, this condition may be violated because of statistical and systematic errors in the pipeline's reconstructed signal parameters, as well as bias and limited accuracy of the ML algorithm. The approach discussed below avoids the occurrence of this inconsistency.

The ground truth of observed events is unknown. Therefore, the probabilities $P(\text{HasNS}|\mathbf{A}_X)$ and $P(\text{HasRemnant}|\mathbf{A}_X)$ cannot be calculated from observations. However, estimators for $P(\text{HasNS}|\mathbf{A}_X)$ and $P(\text{HasRemnant}|\mathbf{A}_X)$ can be calculated from synthetic events under the assumption that these events are a faithful representation of real observations.

Consider a data set of N simulated events \mathbf{X}'_i , $D = \{\mathbf{X}'_i \otimes \mathbf{L}(\mathbf{X}'_i)\}$, where $i = 1 \dots N$ and \mathbf{L} is a map from \mathbf{X}' to a vector space that defines labels for the `HasNS` and `HasRemnant` ground truths. According to Bayes' theorem, $P(\text{HasNS}|\mathbf{A}_X)$ can be written as

$$P(\text{HasNS}|\mathbf{A}_X) = \frac{P(\mathbf{A}_X|\text{HasNS})P(\text{HasNS})}{P(\mathbf{A}_X)}, \quad (1)$$

where $P(\mathbf{A}_X|\text{HasNS})$ is the likelihood of observing the classifier's outcome given an event with a NS in the system, $P(\text{HasNS})$ is the probability that a system includes a NS, and $P(\mathbf{A}_X)$ is the probability of observing the classifier outcome \mathbf{A}_X . The probability $P(\text{HasNS}|\mathbf{A}_X)$ can be approximated as:

$$\begin{aligned} P(\text{HasNS}|\mathbf{A}_X) &\simeq P(\text{HasNS}_+|\mathbf{A}_{X'}) \\ &= \frac{P(\mathbf{A}_{X'}|\text{HasNS}_+)P(\text{HasNS}_+)}{P(\mathbf{A}_{X'})}, \end{aligned} \quad (2)$$

where $\text{HasNS}_+ = \mathbf{L}[\mathbf{X}'(\text{HasNS:TRUE})]$ is a label that uniquely identifies elements in D with positive `HasNS` ground truth, \mathbf{X}' is an element in D , and $\mathbf{A}_{X'}$ is the outcome of the classifier on \mathbf{X}' . The probability $P(\text{HasRemnant}|\mathbf{A}_X)$ can be approximated as:

$$\begin{aligned} P(\text{HasRemnant}|\mathbf{A}_X) &= P(\text{HasRemnant}|\text{HasNS}, \mathbf{A}_X)P(\text{HasNS}|\mathbf{A}_X) \\ &\simeq P(\text{HasRemnant}_+|\mathbf{A}_{X''})P(\text{HasNS}_+|\mathbf{A}_{X'}), \end{aligned} \quad (3)$$

where $\text{HasRemnant}_+ = \mathbf{L}[\mathbf{X}'(\text{HasRemnant:TRUE})]$ is a label that uniquely identifies elements in D with positive `HasRemnant` ground truth and $\mathbf{X}'' = \mathbf{X}'(\text{HasNS:TRUE})$.

To evaluate Eqs. (2) and (3) with an ML classifier, the synthetic data set is divided into two subsets, $D = D_R \oplus D_S$. The D_R subset is used for algorithm training and validation. The D_S subset is used to estimate the probabilities. Following customary practice, throughout this paper we use a 70% – 30% split for D_R and D_S , respectively.

The choice of the labeling scheme and the algorithm's outcome depend on the ML algorithm characteristics.

Throughout this paper we implement a multi-label classification scheme, where each element in D is classified into n mutually exclusive categories that uniquely define the n possible physical states of the system. The classifier outcome can then be chosen as a two-dimensional vector space $\mathbf{A}_{\mathbf{X}'} \subset \mathbb{R}^n$. This scheme allows the calculation of Eqs. (2) and (3) with a single training process. In the problem at hand, there are three possible physical states. A suitable labeling is

$$\begin{aligned} \mathbf{L}[\mathbf{X}'(\text{HasNS:FALSE})] &= 0 \\ \mathbf{L}[\mathbf{X}'(\text{HasNS:TRUE}, \text{HasRemnant:FALSE})] &= 1 \\ \mathbf{L}[\mathbf{X}'(\text{HasNS:TRUE}, \text{HasRemnant:TRUE})] &= 2. \end{aligned} \quad (4)$$

With this labeling, $\text{HasRemnant}_+ = 2$ and $\text{HasNS}_+ = 1 \cup 2$. Therefore a natural choice for the algorithm outcome is

$$\mathbf{A}_{\mathbf{X}'} = (f_1 + f_2, f_2) \subset (f_0, f_1, f_2), \quad (5)$$

where $f_0(\mathbf{X}') = 1 - f_1(\mathbf{X}') - f_2(\mathbf{X}')$, $f_1(\mathbf{X}')$, and $f_2(\mathbf{X}')$ are the fractions of KNN neighbors or RF trees that predict the event to have labels 0, 1, and 2, respectively.

The factors on the right-hand side of Eqs. (2) and (3) can be obtained from D_S once the algorithm has been trained on D_R . For example, for the KNN and RF scheme described earlier, the factors in Eq. (2) can be estimated as

$$\begin{aligned} P(\text{HasNS}_+) &= \frac{N_{\text{HasNS}_+}}{N_s}, \\ P(\mathbf{A}_{\mathbf{X}'} | \text{HasNS}_+) &= \frac{N_{\text{HasNS}_+}^+(f_1 + f_2)}{N_{\text{HasNS}_+}}, \\ P(\mathbf{A}_{\mathbf{X}'}) &= \frac{N_{\text{HasNS}_+}^+(f_1 + f_2) + N_{\text{HasNS}_+}^-(f_1 + f_2)}{N_s}, \end{aligned} \quad (6)$$

where $N_s = \dim(D_S)$, N_{HasNS_+} is the number of events in D_S with label HasNS_+ , and $N_{\text{HasNS}_+}^+(f_1 + f_2)$ and $N_{\text{HasNS}_+}^-(f_1 + f_2)$ are the number of events in D_S that are correctly and incorrectly classified as HasNS_+ by the outcome $f_1 + f_2$, respectively. The first factor on the right-hand side of Eq. (3) can be evaluated similarly to Eq. (2) by replacing HasNS with HasRemnant and restricting D_S to elements with HasNS_+ label.

The probability estimators are generally noisy because they are evaluated on a finite data set. Smooth probability functions can be obtained by mapping them from the $(0, 1)$ space to the real line with a logistic function, smoothing them with a Savitzky-Golay filter, fitting them with Gaussian process regression (GPR), and finally mapping them back to the $(0, 1)$ space.

Both $P(\text{HasNS} | \mathbf{A}_{\mathbf{X}})$ and $P(\text{HasRemnant} | \mathbf{A}_{\mathbf{X}})$ depend on the EOS that is used to label the synthetic events. As the true EOS of matter at NS densities is unknown, in order to minimize the systematics that arise in adopting a specific EOS we consider a set of 23 different EOS and marginalize Eqs. (2) and (3) over them. The marginalized probabilities $P_M(\text{HasNS} | \mathbf{A}_{\mathbf{X}})$ and $P_M(\text{HasRemnant} | \mathbf{A}_{\mathbf{X}})$ are defined as

$$P_M(I | \mathbf{A}_{\mathbf{X}}) = \frac{\sum_J \beta_J P_J(I | \mathbf{A}_{\mathbf{X}})}{\sum_J \beta_J}, \quad (7)$$

where $I = \text{HasNS}$ or HasRemnant , $P_J(I | \mathbf{A}_{\mathbf{X}})$ ($J = 1, \dots, 23$) are the Bayesian probabilities in Eqs. (2) and (3) calculated from the data set D_S with labels assigned according to the J -th EOS, and β_J are Bayes' factors [54]. The probabilities $P_J(I | \mathbf{A}_{\mathbf{X}})$ in Eq. (7) can be tabulated and used to compute the marginalized probabilities $P_M(\text{HasNS} | \mathbf{A}_{\mathbf{E}})$ and $P_M(\text{HasRemnant} | \mathbf{A}_{\mathbf{E}})$ for any new event \mathbf{E} with algorithm outcome $\mathbf{A}_{\mathbf{E}}$.

B. Data Set

We use a large data set D of simulated BNS, NSBH, and BBH events that was first used for the space-time volume sensitivity analysis of the LVK GstLAL search [38–40] and later employed in Ref. [50]. This allows us to directly compare the performance of the various algorithms and the new labeling scheme to the performance of the KNN algorithm that is deployed in the current LVK observing run.

The simulated signals are coherently injected in two-detector data from the O2 LVK observing run. The injection population is built with uniform/loguniform distribution of component masses whereas the component spins are aligned and injected according to isotropic distributions. Further details on the waveforms and injection parameters can be found in Ref. [50]. The data set D includes approximately 200,000 injected signals that are recovered by the GstLAL pipeline with a false alarm rate (FAR) $\leq 1/\text{month}$. The RF and KNN algorithms are trained and tested on the injected and recovered intrinsic source properties (primary and secondary masses and spins) and on the recovered signal-to-noise ratio (SNR).

C. Labeling Scheme

To label the synthetic data set $D = D_R \oplus D_S$, we follow the practice in use in the LVK and identify an event with HasNS:TRUE when at least one of the injected component masses is less than the maximum NS mass allowed by the EOS. The value of the maximum NS mass ranges from $1.922 M_\odot$ to $2.753 M_\odot$ across the various EOS. The lowest and largest maximum NS masses correspond to the BHF_BBB2 and MS1_PP EOS, respectively. We will highlight these two cases together with the SLy EOS, which is the most accepted EOS in the astrophysics community. We set the HasRemnant label as HasRemnant:TRUE and HasRemnant:FALSE for BNS and BBH systems, respectively. The value of the HasRemnant label for NSBH events depends on the EOS of the NS. To identify the HasRemnant event class for NSBH systems, we follow Ref. [50] and apply Eq. (4) from Ref. [46], colloquially known as the *Foucart formula*.

The Foucart formula is an empirical fit that predicts the total mass of the accretion disk, the tidal tail, and the ejected mass from the final BH. The main parameters of the fit are the compactness of the NS, the NSBH

binary system's symmetric mass ratio, and the normalized innermost stable circular orbit (ISCO) radius. The tidal disruption of the NS is affected by the mass and spin of the BH. A highly spinning, low-mass BH's small ISCO allows the NS to inspiral closer to the BH and its tidal force to tear the NS apart, resulting in matter ejecta. If the tidal forces are weak or the NS is very compact, the BH will swallow the NS and there will be no remnant mass.

Different EOSs have different thresholds for the mass of the remnant. We label events with inferred masses less than this threshold as `HasRemnant:TRUE`. For events with component masses between ~ 2.5 and $3.5M_\odot$, the stiffness of the EOS is the main factor determining the `HasRemnant` label.

IV. RESULTS

In this section, we first discuss the performance of the trained RF and KNN classifiers on the testing data set D_S and use the latter to calculate the Bayesian probabilities $P_M(I|\mathbf{A})$. Then we evaluate $P_M(I|\mathbf{A})$ on two independent data sets. The first set includes a population of simulated CBC events that were injected in the real-time replay of O3 data and was used for the LVK Mock Data Challenge (MDC) [55]. The second set contains the confident LVK O3 detections that are reported in LVK's GWTC-3 catalog [4].

A. Performance on the O2 Testing Set

We assess the performance of the classifiers by measuring the TPR and the false positive rate (FPR) of the events in D_S . We present our findings as ROC curves that illustrate how the TPR varies for various score thresholds as a function of the FPR.

The `HasNS` and `HasRemnant` ROC curves for the KNN algorithm are displayed in the left and right panels of Fig. 1, respectively. Figure 2 displays the analogous curves for the RF classifier. The ROC curves for the 23 EOS are plotted in gray, with three of them highlighted in color: `BHF_BBB2`, the EOS with the lowest maximum mass for the NS; `MS1_PP`, the EOS with the largest maximum mass for the NS; and `SLy`, which allows for a maximum mass of $2.05M_\odot$ and is the standard EOS used in LVK low-latency investigations [54]. The markers denote different thresholds for the algorithm scores.

The two classifiers perform consistently across all EOSs. The TPR for a score threshold of 0.5 is around 0.99 for both `HasNS` and `HasRemnant`. A comparison of the `HasNS` and `HasRemnant` ROC curves for each algorithm shows that the FPR for `HasNS` is generally higher than the FPR for `HasRemnant` at a given threshold. Thus, the algorithms typically do a better job in classifying `HasRemnant` than `HasNS`. Separate comparisons of the KNN and RF ROC curves for `HasNS` and `HasRemnant` reveal that at a given

threshold, RF produces slightly higher TPR and lower FPR than KNN.

B. Bayesian Probabilities for the O3 Sets

After the algorithms have been trained and tested, we compute the Bayesian probabilities defined in Sec. III A in terms of their outcomes. Equations (2) and (3) must be assessed on a data set independent of the training data set, as stated in Sec. III A. To do so, we employ D_S .

The KNN and RF probability estimators are shown for each of the 23 EOS in Figs. 3 and 4, respectively. As expected, the `HasNS` and `HasRemnant` probabilities increase with the fractions of KNN neighbors (RF trees). Local fluctuations in the probabilities are due to noise arising from the finiteness of the data set.

The probabilities in Figs. 3 and 4 can be tabulated and used to compute the marginalized probabilities $P_M(\text{HasNS}|\mathbf{A}_E)$ and $P_M(\text{HasRemnant}|\mathbf{A}_E)$ as in Eq. (7). To evaluate the method, we classify the events from the MDC data set and compute the ROC curves based on the ground truth using Bayesian probability (rather than score) thresholds. The ROC curves are shown in Figs. 5 and 6 for KNN and RF, respectively. In contrast to the O2 data set, the MDC set contains outputs from four matched-filtering pipelines (GstLAL [38–40], PyCBC [41, 56], SPIIR [43], and MBTA [42]). Therefore, we present separate ROC curves for these pipelines.

In the case of `HasNS`, KNN yields a TPR between 0.95 and 0.98 and an FPR smaller than 0.20 for a probability threshold of 0.5 across all pipelines, with the exception of SPIIR. It is not surprising that our classifier performs poorly on SPIIR triggers. A similar result has been reported by other investigations [55]. Because the algorithm was not trained on multiple pipelines, a decrease in performance on triggers recovered by pipelines other than the training pipeline is to be expected. Even though the ML algorithms are generally portable across pipelines and data sets, accurate results critically depend on the training set's faithful representation of the observations. In regard to `HasRemnant`, KNN yields a TPR around 0.975 and an FPR slightly higher than 0.2 for the same threshold across all pipelines, with the exception of GstLAL. RF's results are similar to KNN's results. The RF ROC curves for `HasNS` typically have steeper slopes than for KNN, resulting in a comparable TPR but a lower FPR at a given threshold. In the case of `HasRemnant`, RF performs similarly to KNN for GstLAL but worse for the other pipelines.

A few interesting results are worth mentioning. On the MDC set, both algorithms perform better for `HasNS` than `HasRemnant`, whereas on the O2 set, the reverse is true (see Figs. 1 and 2). KNN performs better than RF on `HasRemnant`, but does worse on `HasNS`. However, on events recovered by GstLAL, the pipeline on which the algorithms have been trained, both algorithms exhibit comparable (high) performance. This seems to indicate

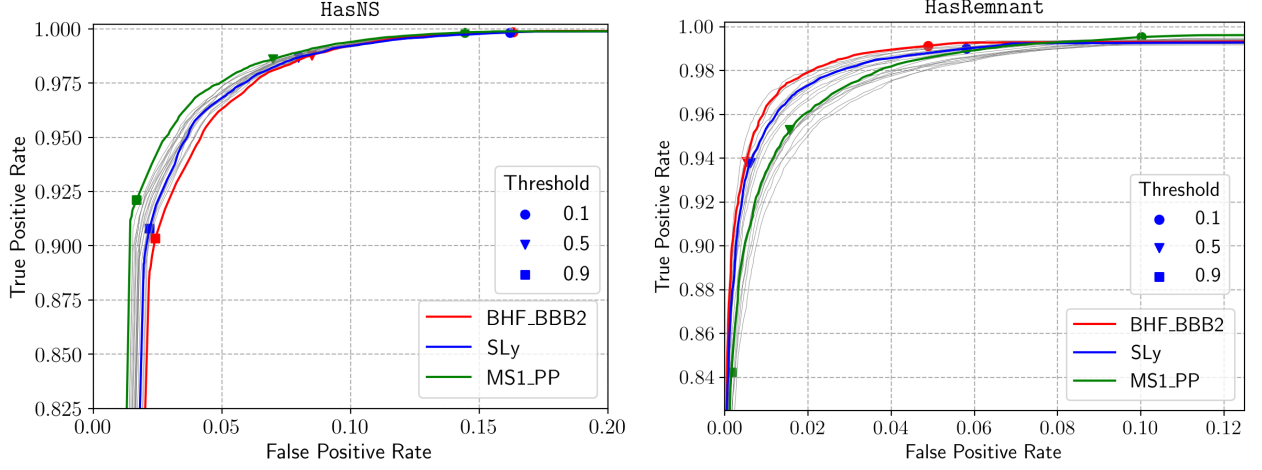


FIG. 1. ROC curves obtained from the O2 testing data set D_S for the KNN classifier (left: **HasNS**, right: **HasRemnant**). The curves for the 23 different EOSs are displayed in gray, with the curves for **BHF_BBB2**, **MS1_PP**, and **SLy** highlighted in red, green, and blue, respectively. The circle, triangle, and square markers denote score thresholds of 0.1, 0.5, and 0.9, respectively.

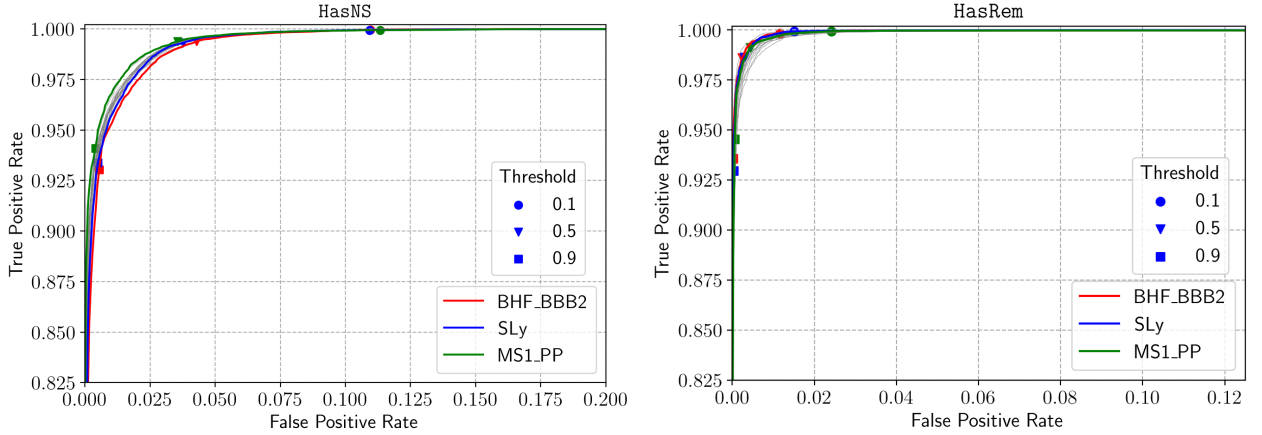


FIG. 2. ROC curves obtained from the O2 testing data set D_S for the RF classifier (left: **HasNS**, right: **HasRemnant**). The curves for the 23 different EOSs are displayed in gray, with the curves for **BHF_BBB2**, **MS1_PP**, and **SLy** highlighted in red, green, and blue, respectively. The circle, triangle, and square markers denote score thresholds of 0.1, 0.5, and 0.9, respectively.

that when used with other pipelines, RF is less flexible than KNN. The conclusions provide more details about this and a possible explanation for this effect.

Finally, we apply the method to derive Bayesian probabilities for the events in the LVK GWTC-3 catalog [4]. In Table I we report the results for some of the most significant GWTC-3 events, labeled with their event ID. The $P_M(\text{HasNS}|\mathbf{A_E})$ and $P_M(\text{HasRemnant}|\mathbf{A_E})$ probabilities for GW170817 and GW190425, the two confirmed BNS detections are ~ 1 as expected. The probabilities for GW190426 and GW200115 (NSBH mergers) are $P_M(\text{HasNS}|\mathbf{A_E}) \sim 1$ and $P_M(\text{HasRemnant}|\mathbf{A_E}) < 10^{-3}$. The two remaining significant events with non-zero probabilities are GW190814 and GW190924. These events were reported as high mass-ratio BBH mergers.

The fact that the system's component masses differ greatly from one another can be used to explain why

$P_M(\text{HasNS}|\mathbf{A_E})$ for these events is not zero. In particular, the discrepancy between RF and KNN for GW190814 can be understood from the different ways the two algorithms operate. RF applies hard cuts on decision trees to evaluate its outcome. KNN looks at the fractions of neighbors surrounding the event. The detection pipeline returned a secondary mass compatible with an NS for three of the 23 EOS. However, since the region of the parameter space close to the mass gap, i.e., the region between high NS masses and low BH masses, is not well covered in the O2 training data set, KNN overestimates the effect of the three EOS predicting a secondary mass in the NS region.

Figures 7 and 8 show parameter sweeps in the space of the binary component masses for the KNN and RF Bayesian probabilities, respectively. Different rows correspond to different values of the component spins. Both algorithms perform in a similar way for $P_M(\text{HasNS}|\mathbf{A_E})$.

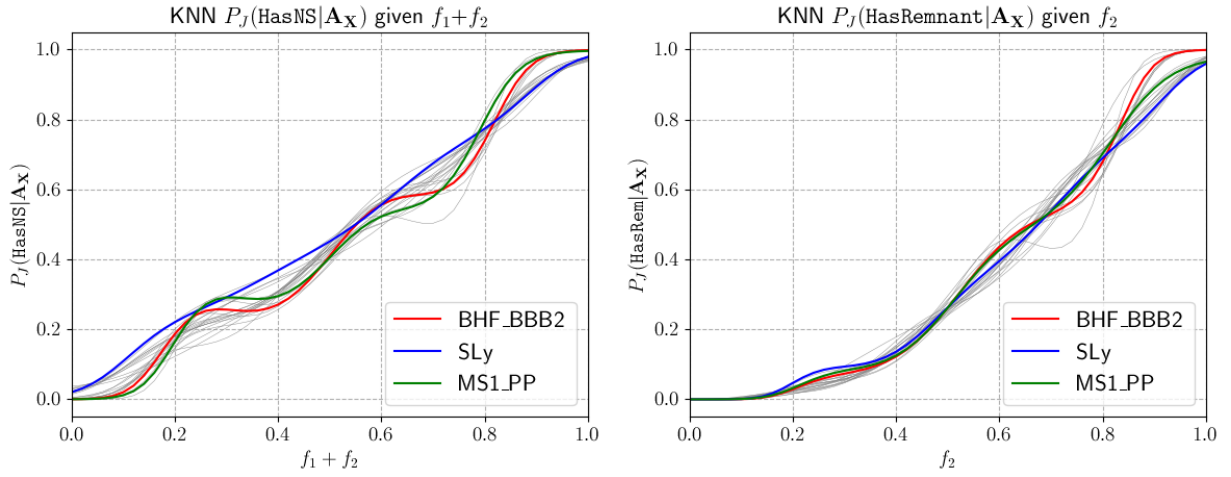


FIG. 3. Left panel: **HasNS** Bayesian probability curves for the 23 EOS as a function of the fraction of KNN neighbors $f_1 + f_2$. Right panel: **HasRemnant** Bayesian probability curves as a function of the fraction of KNN neighbors f_2 . Curves for the BHF_BBB2, MS1_PP, and SLy EOSs are highlighted in red, green, and blue, respectively. The probabilities show an increasing trend as the fraction of neighbors increases. Non-monotonic fluctuations are due to the data set's finite size.

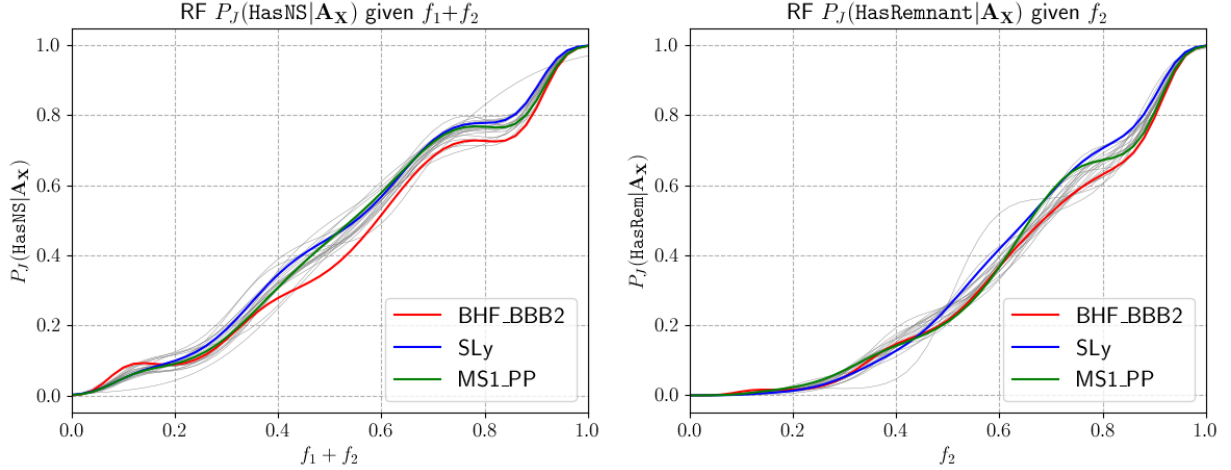


FIG. 4. Left panel: **HasNS** Bayesian probability curves for the 23 EOS as a function of the fraction of RF trees $f_1 + f_2$. Right panel: **HasRemnant** Bayesian probability curves for **HasRemnant** as a function of the fraction of RF Trees f_2 . Curves for the BHF_BBB2, MS1_PP, and SLy EOSs are highlighted in red, green, and blue, respectively. The probabilities show an increasing trend as the fraction of trees increases. Non-monotonic fluctuations are due to the data set's finite size.

event ID	$P_M(\text{HasNS} \mathbf{A_E})$		$P_M(\text{HasRemnant} \mathbf{A_E})$	
	RF	KNN	RF	KNN
GW170817	0.998	0.989	0.997	0.985
GW190425	0.998	0.989	0.997	0.985
GW190426	0.997	0.985	$< 10^{-3}$	$< 10^{-3}$
GW190814	0.042	0.567	$< 10^{-3}$	$< 10^{-3}$
GW190924	0.012	0.054	$< 10^{-3}$	$< 10^{-3}$
GW200115	0.998	0.989	$< 10^{-3}$	$< 10^{-3}$

TABLE I. Bayesian probabilities of a few significant GW events from the GWTC-3 catalog. GW170817 and GW190425, GW190426 and GW200115, and GW190814 and GW190924 were determined to be BNS, NSBH, and BBH mergers, respectively. The probability values in the table are rounded to three decimal figures.

However, the parameter sweeps for $P_M(\text{HasNS}|\mathbf{A_E})$ for KNN are noisier than RF for large primary masses. As was noted above, the KNN algorithm operates by looking at the closest neighbors. If neighbors with different labels are present in the region of interest, the outcome is bound to be noisy. The RF algorithm applies hard selection cuts to primary masses. This results in a more uniform probability. Changes in spin seem to not significantly affect the outcome. Similar behaviors for KNN and RF can also be observed in the case of $P_M(\text{HasRemnant}|\mathbf{A_E})$. As expected from the Foucart formula, $P_M(\text{HasRemnant}|\mathbf{A_E})$ increases with the primary mass for large primary spins, and the region with $P_M(\text{HasRemnant}|\mathbf{A_E}) \sim 1$ is included in the region where $P_M(\text{HasNS}|\mathbf{A_E}) \sim 1$.

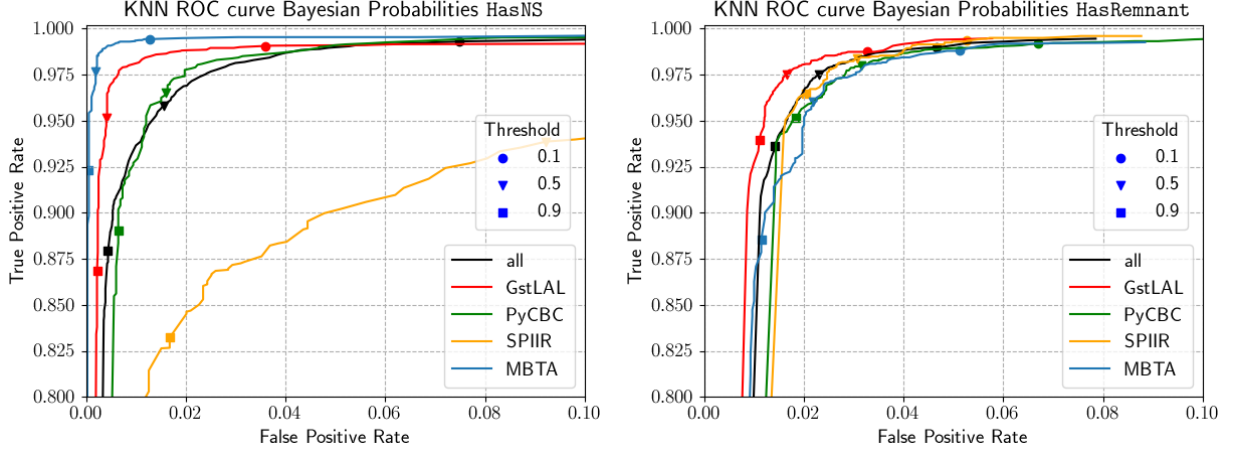


FIG. 5. ROC curves obtained from the O3 MDC data set for the KNN classifier (left: **HasNS**, right: **HasRemnant**). The different LVK matched-filtering pipelines are indicated by different colors (GstLAL: red; PyCBC: green; gold: SPIIR; blue: MBTA). The results for all pipelines are shown in black. The circle, triangle, and square markers denote probability thresholds of 0.1, 0.5, and 0.9, respectively.

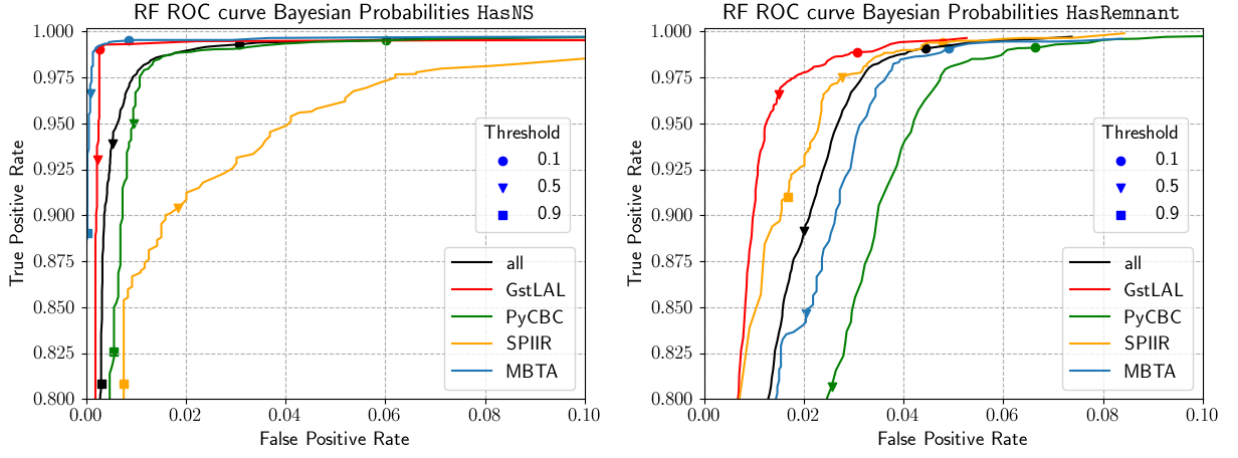


FIG. 6. ROC curves obtained from the O3 MDC data set for the RF classifier (left: **HasNS**, right: **HasRemnant**). The different LVK matched-filtering pipelines are indicated by different colors (GstLAL: red; PyCBC: green; gold: SPIIR; blue: MBTA). The results for all pipelines are shown in black. The circle, triangle, and square markers denote probability thresholds of 0.1, 0.5, and 0.9, respectively.

V. CONCLUSIONS

In this paper, we have presented a new scheme for real-time classification of GW CBC signals detected by the LVK detectors. The method uses the output of the LVK low-latency pipelines to identify whether the GW source progenitor contains a NS (**HasNS**) and a post-merger matter remnant is produced in the merger (**HasRemnant**). Estimates of these metrics are included in public alerts for candidate GW events issued by the LVK. Determining these metrics in low latency is crucial to enabling coincident MMA observations of GW and EM signatures.

We have assessed the viability and measured the performance of two classifiers, KNN and RF, on two sets of real detector data augmented with synthetic GW injections

of GW signals that were generated for space-time volume sensitivity analyses of O2 LVK GW searches [50] and an MDC real-time replay of O3 data [55].

One important novel ingredient of the proposed scheme is the computation of Bayesian probabilities for **HasNS** and **HasRemnant**. Until now, the information that has been passed to astronomers in public alerts has been in the form of binary classification scores for these metrics. Here, we provide a method to compute **HasNS** and **HasRemnant** as actual probabilities that the GW source includes a neutron star and post-merger matter remnant. Therefore, our scheme provides more direct and easily interpretable information to aid the community of astronomers in deciding whether to follow up on GW candidate events with EM observatories.

KNN

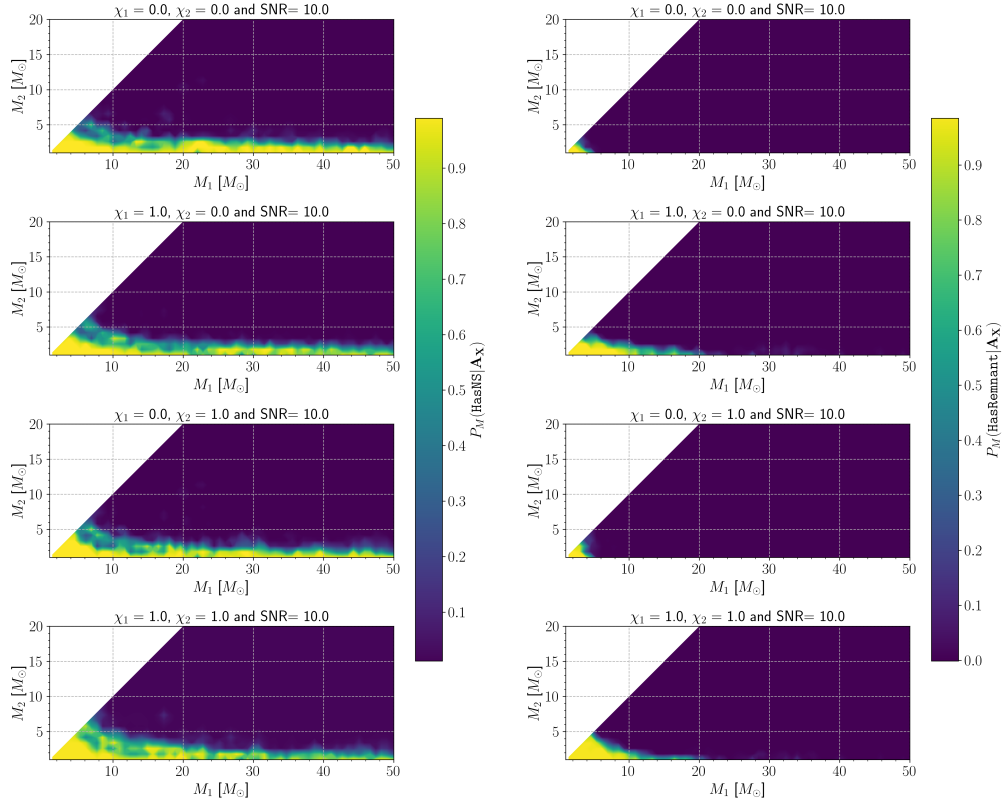


FIG. 7. Parameter sweeps for $P_M(\text{HasNS}|\mathbf{A}_E)$ (left panels) and $P_M(\text{HasRemnant}|\mathbf{A}_E)$ (right panels) for the KNN algorithm. M_1 and M_2 are the primary and secondary component masses of the binary. χ_1 and χ_2 are their effective spins. The SNR is fixed to 10.

To construct the Bayesian probabilities for **HasNS** and **HasRemnant**, we train and test the classifiers on the O2 data set following the customary 70% – 30% split between training and testing data. After evaluating the performance of the classifiers with standard ROC curves, we use the testing set to generate numerical Bayesian probability expressions for the models. This minimizes potential bias that may result from the use of data sets with different properties while ensuring that the Bayesian fits are built with data that is independent of the data used for training the classifiers. The effectiveness of the Bayesian fits is then evaluated on fully independent data sets using the O3 set and real detections.

Both our methods outperform the specific KNN algorithm implementation that is currently used in the LVK low-latency infrastructure when tested on the (GstLAL-only) O2 set of recovered injections, with RF outperforming KNN for both **HasNS** and **HasRemnant**. When tested on the O3 set, both algorithms improve on **HasNS** while underperforming on **HasRemnant**. In this case, KNN

outperforms RF, which exhibits more variation across different pipelines. If only the injections recovered by GstLAL are considered in O3, the O3 results of both RF and KNN are consistent with O2. RF’s performance on O3 events recovered by other pipelines, on the other hand, is noticeably lower. This appears to imply that RF is less portable than KNN across different data sets and pipelines. The different ways RF and KNN operate, as well as the different characteristics of the sets, may explain their behavior.

The RF classifier is a decision tree-based classifier that sets decision rules by implementing specific cuts (conditions) on input features. The KNN algorithm implements decision rules by computing the nearest neighbors of input features in the parameter space for the data point of interest. RF is designed to construct hard boundaries based on input parameters, whereas the KNN algorithm is designed to produce an outcome based on differences between features. As a result, the RF algorithm’s nature may make it more suitable for classifying events with

RF

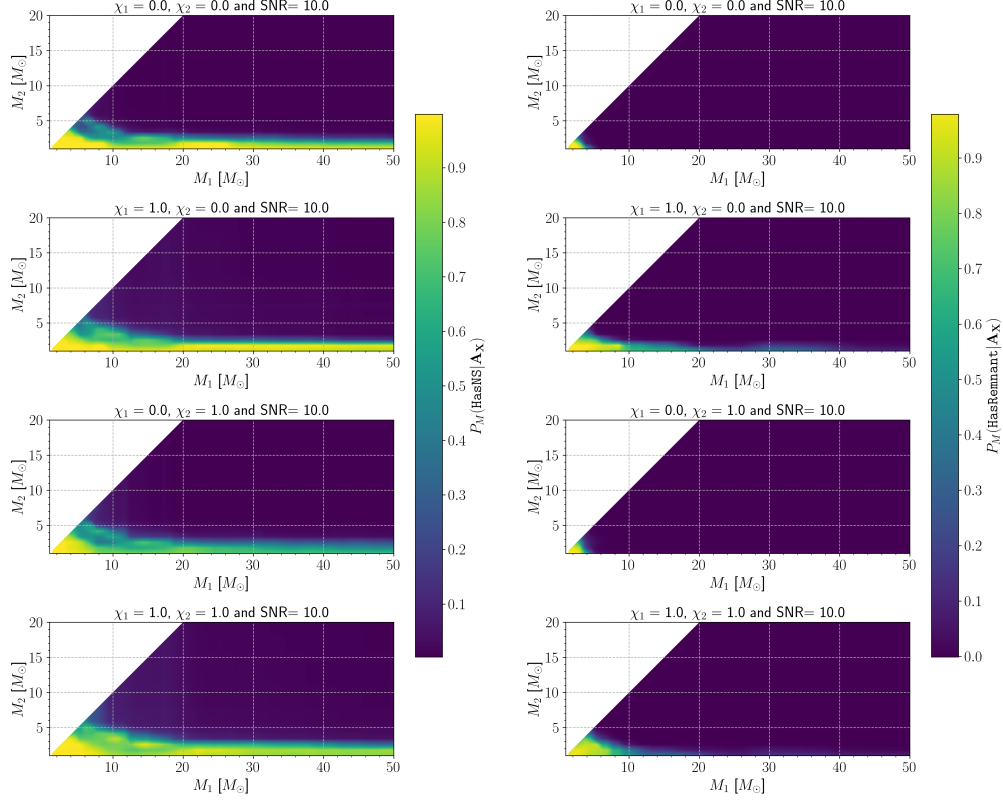


FIG. 8. Parameter sweeps for $P_M(\text{HasNS}|\mathbf{A}_E)$ (left panels) and $P_M(\text{HasRemnant}|\mathbf{A}_E)$ (right panels) for the RF algorithm. M_1 and M_2 are the primary and secondary component masses of the binary. χ_1 and χ_2 are their effective spins. The SNR is fixed to 10.

HasNS, which is based on a well-defined, hard boundary between positive and negative outcomes, such as the secondary mass value. To distinguish between systems with zero and nonzero post-remnant matter in **HasRemnant**, the algorithms must learn Foucart’s fit from the recovered parameters. Foucart’s formula is dependent on the EOS under consideration, as well as the pipeline that recovers the injection. Because RF and KNN are trained on injections that are only recovered by GstLAL, RF is more affected than KNN.

This work provides an improved scheme to implement Bayesian probabilities for **HasNS** and **HasRemnant** classification of candidate events that would be straightforward to deploy in the existing LVK infrastructure. Our method can also be easily extended to other properties of GW signals that are being or may be released in low latency, such as **HasMassGap** among other data products. Other future extensions of this work include improving algorithm training and Bayesian fit estimation with updated data sets of simulated injections in LVK O4 data gener-

ated with different pipelines and with better coverage of the mass gap region than the O2 data set. It would also be worthwhile to investigate the use of additional ML classifiers that could further improve the process’s accuracy, reduce the need for computational resources, and decrease latency. Finally, a similar infrastructure could be designed and deployed to aid in the rapid parameter estimation of pipeline outputs, but with a focus on feature regression rather than classification. This latter line of investigation will be presented in a future publication.

ACKNOWLEDGMENTS

We are very grateful to the authors of Ref. [50] for fruitful discussions and for sharing their work that helped us to directly compare our methods to those used in LVK’s O3 observing run. We would also like to thank the many other colleagues of the LIGO Scientific Collaboration and the Virgo Collaboration who have provided invaluable

help over the years and, in particular, Tito Dal Canton, Thomas Dent, and Shaon Ghosh for their useful comments during the internal LVK review period.

This work is based upon work supported by the LIGO Laboratory which is a major facility fully funded by the National Science Foundation. We are grateful for computational resources provided by the LIGO Laboratory and supported by the U.S. National Science Foundation Awards PHY-0757058 and PHY-0823459.

M.B. is partially supported by the Spanish Agencia Estatal de Investigación grant PID2020-118236GB-I00. M.M.T. is partially supported by the Ministerio de Universidades de España (Spanish Ministry of Universities) through the “Ayuda para la Formación de Profesorado Universitario” (FPU) grant FPU19/01750, by the Spanish Agencia Estatal de Investigación grants PGC2018-095984-B-I00 and PID2021-125485NB-C21 funded by MCIN/AEI/10.13039/501100011033 and the European Regional Development Fund (ERDF) “A way of making Europe,” and by the Generalitat Valenciana (Prometeo grant CIPROM/2022/49). S.S.C. and Y.Z. are partially supported by the U.S. National Science Foundation under awards PHY-2011334 and PHY-2308693. M.C. is partially supported by the U.S. National Science Foundation under awards PHY-2011334, PHY-2219212 and PHY-2308693. L.M.Z. is partially supported by the MSSGC Graduate Research Fellowship, awarded through the NASA Cooperative Agreement 80NSSC20M0101. D.T. is partially supported by the Spanish Agencia Estatal de Investigación grant PID2021-125485NB-C21 funded by MCIN/AEI/10.13039/501100011033 and ERDF “A way of making Europe,” and by the Generalitat Valenciana (Prometeo grant CIPROM/2022/49).

M.W.C. acknowledges support from the National Science Foundation with grant numbers PHY-2308862 and OAC-2117997. A.T. acknowledges support from the National Science Foundation with grant numbers PHY-

2010970 and OAC-2117997.

This research was initiated by M.B., M.M.T., S.A., M.C., L.M.Z., D.T., and Y.Z. during their stay at the Institute of Pure and Applied Mathematics (IPAM), University of California Los-Angeles (UCLA). IPAM is partially supported by the National Science Foundation through award DMS-1925919. These authors would like to thank IPAM and UCLA for their warm hospitality.

Software for this analysis is written in Python 3.x [57] and uses standard Open Source libraries and community-contributed modules from the Python Package Index (PyPI) repository [58] including `numpy` [59], `scipy` [60], `pandas` [61, 62], `matplotlib` [63], and `sklearn` [64].

This manuscript has been assigned LIGO Document Control Center number P2300338.

Author contribution statement. M.B. and M.M.T. designed the RF and KNN models and their computational framework, respectively, and ran the corresponding analyses. S.S.C. curated the data sets and contributed to the analysis, particularly the comparison with the current LVK KNN implementation. M.C. directed the project. S.A., L.M.Z., D.T., and Y.Z. contributed to all aspects of this work, including but not limited to the design and implementation of the research, data analysis, and manuscript writing. Authorship for the LVK members of the MDC builder’s list is requested in publications resulting from the MDC data set. M.W.C. and A.T. are opt-in members of this list. M.W.C. also provided some comments during the internal LVK review period. The authors gratefully thank the other opt-out members of the MDC builder’s list for creating the set, and/or providing summary statistics based on its results, and making these products available to the LVK collaborations: Sarah Antier, Patrick J. Brockill, Deep Chatterjee, Reed Essick, Shaon Ghosh, Patrick Godwin, Erik Katsavounidis, and Gaurav Waratkar.

-
- [1] B. P. Abbott *et al.* (LIGO Scientific, Virgo), Observation of Gravitational Waves from a Binary Black Hole Merger, *Phys. Rev. Lett.* **116**, 061102 (2016), [arXiv:1602.03837 \[gr-qc\]](#).
 - [2] B. P. Abbott *et al.* (LIGO Scientific, Virgo), GW170817: Observation of Gravitational Waves from a Binary Neutron Star Inspiral, *Phys. Rev. Lett.* **119**, 161101 (2017), [arXiv:1710.05832 \[gr-qc\]](#).
 - [3] B. P. Abbott *et al.* (LIGO Scientific, Virgo), GW170817: Measurements of neutron star radii and equation of state, *Phys. Rev. Lett.* **121**, 161101 (2018), [arXiv:1805.11581 \[gr-qc\]](#).
 - [4] R. Abbott *et al.* (LIGO Scientific, VIRGO, KAGRA), GWTC-3: Compact Binary Coalescences Observed by LIGO and Virgo During the Second Part of the Third Observing Run, (2021), [arXiv:2111.03606 \[gr-qc\]](#).
 - [5] P. Schmidt, Gravitational Waves From Binary Black Hole Mergers: Modeling and Observations, *Front. Astron. Space Sci.* **7**, 28 (2020).
 - [6] A. H. Nitz, S. Kumar, Y.-F. Wang, S. Kastha, S. Wu, M. Schäfer, R. Dhurkunde, and C. D. Capano, 4-OGC: Catalog of Gravitational Waves from Compact Binary Mergers, *Astrophys. J.* **946**, 59 (2023), [arXiv:2112.06878 \[astro-ph.HE\]](#).
 - [7] L. Barack *et al.*, Black holes, gravitational waves and fundamental physics: a roadmap, *Class. Quant. Grav.* **36**, 143001 (2019), [arXiv:1806.05195 \[gr-qc\]](#).
 - [8] M. Ruiz, S. L. Shapiro, and A. Tsokaros, Multimessenger Binary Mergers Containing Neutron Stars: Gravitational Waves, Jets, and γ -Ray Bursts, *Front. Astron. Space Sci.* **8**, 39 (2021), [arXiv:2102.03366 \[astro-ph.HE\]](#).
 - [9] L. Baiotti and L. Rezzolla, Binary neutron star mergers: a review of Einstein’s richest laboratory, *Rept. Prog. Phys.* **80**, 096901 (2017), [arXiv:1607.03540 \[gr-qc\]](#).
 - [10] P. D. Lasky, Gravitational Waves from Neutron Stars: A Review, *Publ. Astron. Soc. Austral.* **32**, e034 (2015), [arXiv:1508.06643 \[astro-ph.HE\]](#).
 - [11] K. Murase and I. Bartos, High-Energy Multimessenger

- Transient Astrophysics, *Ann. Rev. Nucl. Part. Sci.* **69**, 477 (2019), [arXiv:1907.12506 \[astro-ph.HE\]](#).
- [12] R. Ciolfi, Short gamma-ray burst central engines, *Int. J. Mod. Phys. D* **27**, 1842004 (2018), [arXiv:1804.03684 \[astro-ph.HE\]](#).
- [13] R. Abbott *et al.* (LIGO Scientific, VIRGO, KAGRA), Tests of General Relativity with GWTC-3, (2021), [arXiv:2112.06861 \[gr-qc\]](#).
- [14] E. Berti, K. Yagi, and N. Yunes, Extreme Gravity Tests with Gravitational Waves from Compact Binary Coalescences: (I) Inspiral-Merger, *Gen. Rel. Grav.* **50**, 46 (2018), [arXiv:1801.03208 \[gr-qc\]](#).
- [15] E. Berti, K. Yagi, H. Yang, and N. Yunes, Extreme Gravity Tests with Gravitational Waves from Compact Binary Coalescences: (II) Ringdown, *Gen. Rel. Grav.* **50**, 49 (2018), [arXiv:1801.03587 \[gr-qc\]](#).
- [16] M. Isi, M. Giesler, W. M. Farr, M. A. Scheel, and S. A. Teukolsky, Testing the no-hair theorem with GW150914, *Phys. Rev. Lett.* **123**, 111102 (2019), [arXiv:1905.00869 \[gr-qc\]](#).
- [17] P. A. Seoane *et al.* (LISA), Astrophysics with the Laser Interferometer Space Antenna, *Living Rev. Rel.* **26**, 2 (2023), [arXiv:2203.06016 \[gr-qc\]](#).
- [18] E. Barausse *et al.*, Prospects for Fundamental Physics with LISA, *Gen. Rel. Grav.* **52**, 81 (2020), [arXiv:2001.09793 \[gr-qc\]](#).
- [19] A. Piórkowska-Kurpas and M. Biesiada, Testing Quantum Gravity in the Multi-Messenger Astronomy Era, *Universe* **8**, 321 (2022).
- [20] R. Abbott *et al.* (LIGO Scientific, VIRGO, KAGRA), The population of merging compact binaries inferred using gravitational waves through GWTC-3, (2021), [arXiv:2111.03634 \[astro-ph.HE\]](#).
- [21] R. Abbott *et al.* (LIGO Scientific, VIRGO, KAGRA), Constraints on the cosmic expansion history from GWTC-3, (2021), [arXiv:2111.03604 \[astro-ph.CO\]](#).
- [22] J. Aasi *et al.* (LIGO Scientific), Advanced LIGO, *Class. Quant. Grav.* **32**, 074001 (2015), [arXiv:1411.4547 \[gr-qc\]](#).
- [23] F. Acernese *et al.* (VIRGO), Advanced Virgo: a second-generation interferometric gravitational wave detector, *Class. Quant. Grav.* **32**, 024001 (2015), [arXiv:1408.3978 \[gr-qc\]](#).
- [24] B. P. Abbott *et al.* (KAGRA, LIGO Scientific, Virgo, VIRGO), Prospects for observing and localizing gravitational-wave transients with Advanced LIGO, Advanced Virgo and KAGRA, *Living Rev. Rel.* **21**, 3 (2018), [arXiv:1304.0670 \[gr-qc\]](#).
- [25] J. M. Lattimer and D. N. Schramm, Black-hole-neutron-star collisions, *Astrophys. J. Lett.* **192**, L145 (1974).
- [26] L.-X. Li and B. Paczynski, Transient events from neutron star mergers, *Astrophys. J. Lett.* **507**, L59 (1998), [arXiv:astro-ph/9807272](#).
- [27] O. Korobkin, S. Rosswog, A. Arcones, and C. Winteler, On the astrophysical robustness of neutron star merger r-process, *Mon. Not. Roy. Astron. Soc.* **426**, 1940 (2012), [arXiv:1206.2379 \[astro-ph.SR\]](#).
- [28] J. Barnes and D. Kasen, Effect of a High Opacity on the Light Curves of Radioactively Powered Transients from Compact Object Mergers, *Astrophys. J.* **775**, 18 (2013), [arXiv:1303.5787 \[astro-ph.HE\]](#).
- [29] M. Tanaka and K. Hotokezaka, Radiative Transfer Simulations of Neutron Star Merger Ejecta, *Astrophys. J.* **775**, 113 (2013), [arXiv:1306.3742 \[astro-ph.HE\]](#).
- [30] D. Kasen, R. Fernandez, and B. Metzger, Kilonova light curves from the disc wind outflows of compact object mergers, *Mon. Not. Roy. Astron. Soc.* **450**, 1777 (2015), [arXiv:1411.3726 \[astro-ph.HE\]](#).
- [31] B. P. Abbott *et al.* (LIGO Scientific, Virgo, Fermi GBM, INTEGRAL, IceCube, AstroSat Cadmium Zinc Telluride Imager Team, IPN, Insight-Hxmt, ANTARES, Swift, AGILE Team, 1M2H Team, Dark Energy Camera GW-EM, DES, DLT40, GRAWITA, Fermi-LAT, ATCA, ASKAP, Las Cumbres Observatory Group, OzGrav, DWF (Deeper Wider Faster Program), AST3, CAASTRO, VIN-ROUGE, MASTER, J-GEM, GROWTH, JAGWAR, CaltechNRAO, TTU-NRAO, NuSTAR, Pan-STARRS, MAXI Team, TZAC Consortium, KU, Nordic Optical Telescope, ePESTO, GROND, Texas Tech University, SALT Group, TOROS, BOOTES, MWA, CALET, IKI-GW Follow-up, H.E.S.S., LOFAR, LWA, HAWC, Pierre Auger, ALMA, Euro VLBI Team, Pi of Sky, Chandra Team at McGill University, DFN, ATLAS Telescopes, High Time Resolution Universe Survey, RIMAS, RATIR, SKA South Africa/MeerKAT), Multi-messenger Observations of a Binary Neutron Star Merger, *Astrophys. J. Lett.* **848**, L12 (2017), [arXiv:1710.05833 \[astro-ph.HE\]](#).
- [32] I. Arcavi *et al.*, Optical emission from a kilonova following a gravitational-wave-detected neutron-star merger, *Nature* **551**, 64 (2017), [arXiv:1710.05843 \[astro-ph.HE\]](#).
- [33] D. A. Coulter *et al.*, Swope Supernova Survey 2017a (SSS17a), the Optical Counterpart to a Gravitational Wave Source, *Science* **358**, 1556 (2017), [arXiv:1710.05452 \[astro-ph.HE\]](#).
- [34] M. M. Kasliwal *et al.*, Illuminating Gravitational Waves: A Concordant Picture of Photons from a Neutron Star Merger, *Science* **358**, 1559 (2017), [arXiv:1710.05436 \[astro-ph.HE\]](#).
- [35] V. M. Lipunov *et al.*, MASTER Optical Detection of the First LIGO/Virgo Neutron Star Binary Merger GW170817, *Astrophys. J. Lett.* **850**, L1 (2017), [arXiv:1710.05461 \[astro-ph.HE\]](#).
- [36] M. Soares-Santos *et al.* (DES, Dark Energy Camera GW-EM), The Electromagnetic Counterpart of the Binary Neutron Star Merger LIGO/Virgo GW170817. I. Discovery of the Optical Counterpart Using the Dark Energy Camera, *Astrophys. J. Lett.* **848**, L16 (2017), [arXiv:1710.05459 \[astro-ph.HE\]](#).
- [37] N. R. Tanvir *et al.*, The Emergence of a Lanthanide-Rich Kilonova Following the Merger of Two Neutron Stars, *Astrophys. J. Lett.* **848**, L27 (2017), [arXiv:1710.05455 \[astro-ph.HE\]](#).
- [38] S. Sachdev *et al.*, The GstLAL Search Analysis Methods for Compact Binary Mergers in Advanced LIGO's Second and Advanced Virgo's First Observing Runs, (2019), [arXiv:1901.08580 \[gr-qc\]](#).
- [39] C. Messick, K. Blackburn, P. Brady, P. Brockill, K. Cannon, R. Cariou, S. Caudill, S. J. Chamberlin, J. D. E. Creighton, R. Everett, C. Hanna, D. Keppel, R. N. Lang, T. G. F. Li, D. Meacher, A. Nielsen, C. Pankow, S. Privitera, H. Qi, S. Sachdev, L. Sadeghian, L. Singer, E. G. Thomas, L. Wade, M. Wade, A. Weinstein, and K. Wiesner, Analysis framework for the prompt discovery of compact binary mergers in gravitational-wave data, *Phys. Rev. D* **95**, 042001 (2017).
- [40] S. Sachdev *et al.*, An Early-warning System for Electromagnetic Follow-up of Gravitational-wave Events, *Astrophys. J. Lett.* **905**, L25 (2020), [arXiv:2008.04288 \[astro-ph.HE\]](#).

- [41] A. H. Nitz, T. Dal Canton, D. Davis, and S. Reyes, Rapid detection of gravitational waves from compact binary mergers with PyCBC Live, *Phys. Rev. D* **98**, 024050 (2018), [arXiv:1805.11174 \[gr-qc\]](#).
- [42] T. Adams, D. Buskulic, V. Germain, G. M. Guidi, F. Marion, M. Montani, B. Mours, F. Piergiovanni, and G. Wang, Low-latency analysis pipeline for compact binary coalescences in the advanced gravitational wave detector era, *Class. Quant. Grav.* **33**, 175012 (2016), [arXiv:1512.02864 \[gr-qc\]](#).
- [43] Q. Chu *et al.*, SPIIR online coherent pipeline to search for gravitational waves from compact binary coalescences, *Phys. Rev. D* **105**, 024023 (2022), [arXiv:2011.06787 \[gr-qc\]](#).
- [44] S. Klimenko *et al.*, Method for detection and reconstruction of gravitational wave transients with networks of advanced detectors, *Phys. Rev. D* **93**, 042004 (2016), [arXiv:1511.05999 \[gr-qc\]](#).
- [45] F. Foucart, Black Hole-Neutron Star Mergers: Disk Mass Predictions, *Phys. Rev. D* **86**, 124007 (2012), [arXiv:1207.6304 \[astro-ph.HE\]](#).
- [46] F. Foucart, T. Hinderer, and S. Nissanke, Remnant baryon mass in neutron star-black hole mergers: Predictions for binary neutron star mimickers and rapidly spinning black holes, *Phys. Rev. D* **98**, 081501 (2018), [arXiv:1807.00011 \[astro-ph.HE\]](#).
- [47] A. M. Farah, M. Fishbach, R. Essick, D. E. Holz, and S. Galadage, Bridging the Gap: Categorizing Gravitational-wave Events at the Transition between Neutron Stars and Black Holes, *Astrophys. J.* **931**, 108 (2022), [arXiv:2111.03498 \[astro-ph.HE\]](#).
- [48] <https://rtd.igwn.org/projects/userguide/en/v17.1/content.html>.
- [49] F. Pedregosa *et al.*, Scikit-learn: Machine Learning in Python, *J. Machine Learning Res.* **12**, 2825 (2011), [arXiv:1201.0490 \[cs.LG\]](#).
- [50] D. Chatterjee, S. Ghosh, P. R. Brady, S. J. Kapadia, A. L. Miller, S. Nissanke, and F. Pannarale, A Machine Learning Based Source Property Inference for Compact Binary Mergers, *Astrophys. J.* **896**, 54 (2020), [arXiv:1911.00116 \[astro-ph.IM\]](#).
- [51] E. Fix and J. L. Hodges, Discriminatory analysis. non-parametric discrimination: Consistency properties, *International Statistical Review / Revue Internationale de Statistique* **57**, 238 (1989).
- [52] T. Cover and P. Hart, Nearest neighbor pattern classification, *IEEE Transactions on Information Theory* **13**, 21 (1967).
- [53] G. Guo, H. Wang, D. Bell, Y. Bi, and K. Greer, Knn model-based approach in classification, in *On The Move to Meaningful Internet Systems 2003: CoopIS, DOA, and ODBASE*, Vol. 2888 (2003) pp. 986–996.
- [54] S. Ghosh, X. Liu, J. Creighton, W. Kastaun, G. Pratten, and I. M. Hernandez, Rapid model comparison of equations of state from gravitational wave observation of binary neutron star coalescences, *Phys. Rev. D* **104**, 083003 (2021), [arXiv:2104.08681 \[gr-qc\]](#).
- [55] S. S. Chaudhary *et al.*, Low-latency gravitational wave alert products and their performance in anticipation of the fourth LIGO-Virgo-KAGRA observing run, (2023), [arXiv:2308.04545 \[astro-ph.HE\]](#).
- [56] T. Dal Canton, A. H. Nitz, B. Gadre, G. S. Cabourn Davies, V. Villa-Ortega, T. Dent, I. Harry, and L. Xiao, Real-time Search for Compact Binary Mergers in Advanced LIGO and Virgo’s Third Observing Run Using PyCBC Live, *Astrophys. J.* **923**, 254 (2021), [arXiv:2008.07494 \[astro-ph.HE\]](#).
- [57] G. Van Rossum and F. L. Drake, *Python 3 Reference Manual* (CreateSpace, Scotts Valley, CA, 2009).
- [58] [Python package index - pypi](#).
- [59] C. R. Harris, K. J. Millman, S. J. van der Walt, R. Gommers, P. Virtanen, D. Cournapeau, E. Wieser, J. Taylor, S. Berg, N. J. Smith, R. Kern, M. Picus, S. Hoyer, M. H. van Kerkwijk, M. Brett, A. Haldane, J. F. del Río, M. Wiebe, P. Peterson, P. Gérard-Marchant, K. Sheppard, T. Reddy, W. Weckesser, H. Abbasi, C. Gohlke, and T. E. Oliphant, Array programming with NumPy, *Nature* **585**, 357 (2020).
- [60] P. Virtanen, R. Gommers, T. E. Oliphant, M. Haberland, T. Reddy, D. Cournapeau, E. Burovski, P. Peterson, W. Weckesser, J. Bright, S. J. van der Walt, M. Brett, J. Wilson, K. J. Millman, N. Mayorov, A. R. J. Nelson, E. Jones, R. Kern, E. Larson, C. J. Carey, Í. Polat, Y. Feng, E. W. Moore, J. VanderPlas, D. Laxalde, J. Perktold, R. Cimrman, I. Henriksen, E. A. Quintero, C. R. Harris, A. M. Archibald, A. H. Ribeiro, F. Pedregosa, P. van Mulbregt, and SciPy 1.0 Contributors, SciPy 1.0: Fundamental Algorithms for Scientific Computing in Python, *Nature Methods* **17**, 261 (2020).
- [61] T. pandas development team, [pandas-dev/pandas: Pandas](#) (2020).
- [62] Wes McKinney, Data Structures for Statistical Computing in Python, in *Proceedings of the 9th Python in Science Conference*, edited by Stéfan van der Walt and Jarrod Millman (2010) pp. 56 – 61.
- [63] J. D. Hunter, Matplotlib: A 2D Graphics Environment, *Comput. Sci. Eng.* **9**, 90 (2007).
- [64] F. Pedregosa, G. Varoquaux, A. Gramfort, V. Michel, B. Thirion, O. Grisel, M. Blondel, P. Prettenhofer, R. Weiss, V. Dubourg, J. Vanderplas, A. Passos, D. Cournapeau, M. Brucher, M. Perrot, and E. Duchesnay, Scikit-learn: Machine learning in Python, *Journal of Machine Learning Research* **12**, 2825 (2011).